Applied Thermal Engineering 257 (2024) 124206

Contents lists available at ScienceDirect

Applied Thermal Engineering

journal homepage: www.elsevier.com/locate/apthermeng

Research Paper

Experimental investigation on heat transfer enhancement of supercritical pressure aviation kerosene in tubular laminar flow by vibration

Yanchen Fu [a,b], Weitong Liu [a,b], Juan Wang [c], Lina Zhang [a,b], Jie Wen [a,b], Hongwei Wu [d], Guoqiang Xu [a,b,*]

[a] Research Institute of Aero-engine, Beihang University, Beijing 100191, China
[b] Collaborative Innovation Center for Advanced Aero-Engine, Beihang University, Beijing 100191, China
[c] AECC Sichuan Gas Turbine Research Institute, Chengdu 610500, China
[d] School of Physics, Engineering and Computer Science, University of Hertfordshire, Hatfield, AL10 9AB, United Kingdom

ARTICLE INFO

Keywords:
Heat transfer enhancement
Vibration
Supercritical aviation kerosene
Laminar flow

ABSTRACT

In advanced aero-engine thermal management systems, aviation kerosene serving as a coolant unavoidably works in a vibration environment. In this article, the laminar heat transfer performance of Chinese aviation kerosene RP-3 flowing through a horizontal micro-tube under various vibration conditions at supercritical pressures was investigated experimentally. The effects of several impact factors such as system pressure, heat flux, mass flux, inlet temperature, vibration acceleration, and vibration frequency on the heat transfer enhancement were explored in a systematic manner. Experimental results indicate that: (i) the vibration could lead to intense thermal and momentum mixing among different boundary layers of tubular laminar flow and significantly strengthens the heat transfer, and the higher *Re* can lead to a stronger enhancement effect. The maximum observed HTER across all experimental data is 2.8, occurring at $x/d = 224.1$ with the inlet temperature of 373 K; (ii) HTER hardly changes with system pressures, exhibiting a maximum relative deviation of 3.9 % at different pressures. Heat transfer enhancement has a strong dependency on heat flux, as the heat flux increases from 36 kW/m^2 to 108 kW/m^2, the average HTC increased by up to 36.4 %; (iii) the HTC and HTER monotonically rise with increasing vibration acceleration. Peak values in HTC and HTER are observed at vibration frequencies of 625 Hz, 191 Hz, and 242 Hz; (iv) vibration has little impact on the thermal acceleration but noticeably weakens the buoyancy close to the outlet area at high heat flux. Two well-predicted correlations for the *Nu* in tubular laminar flow, one with vibration and one without, are proposed.

1. Introduction

Thermal management is a key technology in advanced aircraft, aero-engine, and hypersonic vehicle applications [1]. With the rapid development of the thermal management technology, as a significant potential coolant in cooling channels, the thermodynamic characteristics of the supercritical aviation kerosene have attracted worldwide attention [2–6]. Moreover, laminar flow plays a significant role in advanced aircraft. Laminar flow control systems can greatly reduce flight drag, leading to an increase in cruise efficiency [7,8]. Under icing conditions, thermal pneumatic anti-icing systems use hot bleed air from engines to warm the leading edges of the wings, involving laminar flow heat transfer of air during this process [9,10]. Additionally, aircraft thermal management systems comprise numerous subsystems, such as environmental control systems, electrical power systems, fuel systems, oil systems, and cooling air systems [1], each containing various types of heat exchangers [11,12]. Due to the variability of flight conditions [13], the fluid flow within these heat exchangers may experience laminar, transitional, and turbulent flow regimes. Thus, studying the characteristics of laminar flow heat transfer is also essential. Focusing on the application of Cooled Cooling Air technology [14], Liu et al. [3] investigated the forced, natural, and mixed convective heat transfer characteristics of supercritical n-decane in a tube laminar flow. For regenerative cooling technology, Kimura and Aritomi [15,16] developed a phenomenological method to assess the effectiveness of laminar forced-convective heat transfer between a heated wall and a fluid undergoing endothermic reactions. Regarding the transpiration cooling technology, Liu et al. [17,18] proposed the Navier-Stokes equation in cylindrical coordinates to investigate the impact of the two-dimensional

* Corresponding author at: Research Institute of Aero-engine, Beihang University, Beijing 100191, China.
E-mail address: guoqiang_xu@buaa.edu.cn (G. Xu).

https://doi.org/10.1016/j.applthermaleng.2024.124206
Received 7 May 2024; Received in revised form 18 July 2024; Accepted 17 August 2024
Available online 20 August 2024

Nomenclature

a	Vibration acceleration [m/s^2]
c_p	Isobaric specific heat capacity [kJ/(kg·K)]
d	Tube diameter [mm]
f	Vibration frequency [Hz]
g	Gravity acceleration [9.81 m/s^2]
G	Mass flux [kg/(m^2·s)]
Gr	Grashof number
H	Enthalpy [kJ/kg]
h	Heat transfer coefficient [W/(m^2·K)]
I	Current [A]
k	Thermal conductivity [W/(m·K)]
Kv	Thermal acceleration number
L	Circular tube length [m]
m	Mass flow rate [kg/s]
Nu	Nusselt number
Pr	Prandtl number
P	System pressure [MPa]
q	Heat flux [kW/m^2]
Q	Electric heating power [W]
r	Circular tube radius [m]
Re	Reynolds number
T	Temperature [K]
U	Thermoelectric Potential [mV]

Greek symbols

ε	Uncertainty
μ	Dynamic viscosity [Pa·s]
Φ	Internal heat source [kW/m^3]
ρ	Density [kg/m^3]
$\rho(T)$	Electronic resistivity [Ω·m]

Subscripts

b	Bulk
c	Critical
i	Inlet
in	Inner
out	Outside
pc	Pseudo-critical
s	Without vibration
v	With vibration
w	Wall
x	Distance from the inlet

Abbreviations

CHF	Critical heat flux
HTC	Heat transfer coefficient
HTER	Heat transfer enhancement ratio

laminar transpiration cooling process on the nozzle's flow field. However, in practical application scenarios, the aircraft and aero-engine unavoidably work in a vibration environment, resulting in different flow behavior and heat transfer performance. Therefore, it is imperative to explore how the vibration affects the flow and heat transfer characteristics.

The exploration of vibration influence on the fluid thermodynamic performance can be traced back to the 1960 s [19]. The initiation of research on how vibration influences natural convection heat transfer performance can be attributed to Lemlich et al. [20,21]. Electric hot wires of various diameters were subjected to transverse vibration, and it indicated a substantial increase in the heat transfer coefficient (HTC) with higher amplitudes and frequencies, leading to a four-fold increase in the air and a maximum augmentation of exceeding ten-fold in the water or aqueous glycerine. Currently, vibration is one of the most effective methods for actively enhancing heat transfer [22,23]. Wen [24] conducted vibration effects on heat transfer at frequency parameters of 0.3–10.2 Hz and amplitude parameters of 0.5–8.1 mm. It was found that the HTC could be enhanced with the rise of vibration amplitudes. Amiri et al. [25] examined the impact of cylinder spacing in tandem on the heat transfer performance and their observations indicated that the total Nusselt number increased with rising frequency parameters and Keulegan-Carpenter numbers. Cheng et al. [26] introduced a novel strategy to improve the heat transfer performance by utilizing a newly invented flow-induced vibration device. Their research revealed that the low-flow velocity pulsations could cause vibrations and substantially enhance the heat transfer in nonlinear heat transfer devices. Liu et al. [27] evaluated the effects of sinusoidal vibration and found that the vibration frequency could have a more significant influence on the heat transfer enhancement than that with vibration acceleration. Mohammed et al. [28] explored the thermodynamic performance of a heat exchanger with a turbulator under vibration. They stated that both the heat transfer and pressure drop would increase under vibration, despite the vibration signal type, acceleration, and frequency. The natural convection heat transfer performance over an oscillating elastic fin in a square cavity was investigated numerically by Ghalambaz et al. [29]. They pointed out that increasing the oscillating amplitude of the fin could enhance the heat transfer. As one of the most common working fluids, water has been studied deeply by many researchers. Kim et al. [30] carried out a series of experimental studies on vertical annulus tubes with electrical heating to investigate the vibration impact on the critical heat flux (CHF). They concluded that the mechanical vibration could lead to a CHF enhancement by up to 16.4 %. The vibration amplitude was identified as the most influential parameter in enhancing the CHF, whereas both the mass flux and vibration frequency had no discernible impact. Deaver [31], Penney [32], and Hsieh [33] conducted a series of natural convection heat transfer tests with tube diameters of 0.18 mm, 0.2 mm, and 10 mm at different vibration frequencies and amplitudes in the range of 0–45 Hz and 0–70 mm. They found that the HTC in water under vibration conditions was enhanced by a maximum of 4 times, 5 times, and 0.5 times compared to those at non-vibration states, respectively. Guo et al. [34] performed experiments to examine how the vertical vibration affected a liquid film's flow and heat transfer performance at frequencies between 6 Hz and 30 Hz. Their results showed that the wetness line lengthened under vibration conditions, while its shape changed as the vibration frequency or amplitude increased. Additionally, many efforts have been made on studies with nanofluids. Hosseinian et al. [35] found that vibration could reduce the deposition of nanoparticles in heat transfer tubes which could significantly enhance the HTC of nanofluid. The largest augmentation in HTC was 100 %, achieved at the maximum vibration intensity of 9 m/s^2 and the lowest mass fraction (0.04 %). Zhang et al. [36] found that SiO_2-water based nanofluids under vibration conditions showed better heat transfer performance than that of purified water. With *Re* ranging of 1300–15000, the proportion of heat transfer enhancement could be improved with increasing frequency, and the HTC could be 1.35 times larger than that observed in non-vibration conditions. While under constant vibration frequency, the heat transfer enhancement trend decreased with the increase of *Re*. Moreover, Zuo et al. [37] conducted a series of tests on the heat transfer behavior of aviation kerosene, considering both transition and turbulent flow states under vibration conditions. They observed that the vibrations could significantly improve the heat transfer in the entrance section. It was also observed that as the *Re* increases, the enhancement in heat transfer

diminishes and eventually vanishes as *Re* is higher than 12000. However, their research work did not investigate the heat transfer characteristics of aviation kerosene under laminar flow conditions.

In recent years, the development of numerical simulation technology has provided a powerful tool for a deeper understanding of the mechanisms by which vibration affects heat transfer. Mitsuishi et al. [38] carried out a comprehensive series of direct numerical simulations (DNS) [39] under transverse vibration conditions. They found that *Nu* increased and declined periodically with time, with a total effect of 70 % enhancement in one cycle. According to Rui et al. [40,41], the heat transfer in the tube's internal flow demonstrated a periodic change with half the vibration frequency under cosine vibration conditions. The heat transfer experienced a 1.9 % enhancement compared to that with a non-vibration state at the *Re* of 6140, but when the dimensionless amplitude was increased from 1 to 10, it was enhanced by 35 %. The HTC will increase with increasing distance from the vibration center to the inlet region. The heat transfer performance in viscous non-Newtonian and Newtonian flow under transverse vibration conditions was quantitatively examined by Barigou et al. [42,43]. It was found that the vibration accelerated the development of the temperature profile. Later on, further investigation revealed that the vibration could reduce the inhomogeneity of the radial temperature distribution in the tube, producing an apparent heat transfer enhancement effect. Zhang et al. [44] examined that the *Nu* with periodic wall vibration at low frequency (1–10 Hz) and small vibration amplitude (1–5 mm) could be up to 2.854 times higher than that of a non-vibration tube. Yang et al. [45] investigated the forced convective heat transfer performance of a circular cylinder under two-degree-of-freedom vibration. It was observed that the average *Nu* is increased by 2.46 % and 5.73 % compared with the one-degree-of-freedom vibration and non-vibration condition, respectively.

Among previous literature on vibration effects on heat transfer, the majority of investigations mainly focused on the conventional working fluids, whereas the supercritical fluids were rarely discussed, especially supercritical hydrocarbon fuels that are widely utilized in aero-engines thermal management systems. In order to fill the research gap, the present research will experimentally investigate the vibration-enhanced heat transfer performance of supercritical aviation kerosene RP-3 in a horizontal micro-tube with a focus on a laminar flow regime. The current study will systematically analyze the impact of several impact factors such as system pressure, heat flux, mass flux, fluid inlet temperature, vibration acceleration, and vibration frequency on the heat transfer enhancement level of supercritical RP-3 in a systematic manner. The influence of the vibration on buoyance under inlet laminar flow conditions will be discussed in detail, and two empirical correlations for the *Nu* of laminar state supercritical pressure aviation kerosene RP-3 under vibration and non-vibration conditions will be established.

2. Experimental system

2.1. Experimental apparatus

In the current study, as depicted in Fig. 1, a series of tests are carried out in the aviation kerosene RP-3 flow and heat transfer multi-functional system at both high temperature and pressure. The experimental system comprises four subsystems: the fuel supply system, the heating system, the vibration testing system, and the cooling recovery system.

RP-3 is pumped out of the fuel supply tank and flows through a filter to remove the minor contaminants before entering the precise metering pump (SP6015, 0.01–600 mL/min, 15 MPa). The metering pump not only provides the power for transporting RP-3 but also serves as a pressure stabilizer and safety valve. It features high-response speed pressure regulation capabilities that can stabilize the flow and pressure fluctuations caused by the reciprocating motion of the piston during operation. Fig. 2 shows the variations in RP-3 mass flow rate and pressure over time during the preliminary test, indicating that the mass flow rate fluctuation is within ± 0.1 %, and the pressure fluctuation is within ± 0.3 %. Furthermore, its feedback regulation feature can automatically relieve pressure when the system pressure exceeds 15 MPa, ensuring experimental safety. To meet the requirements for a wide range of inlet

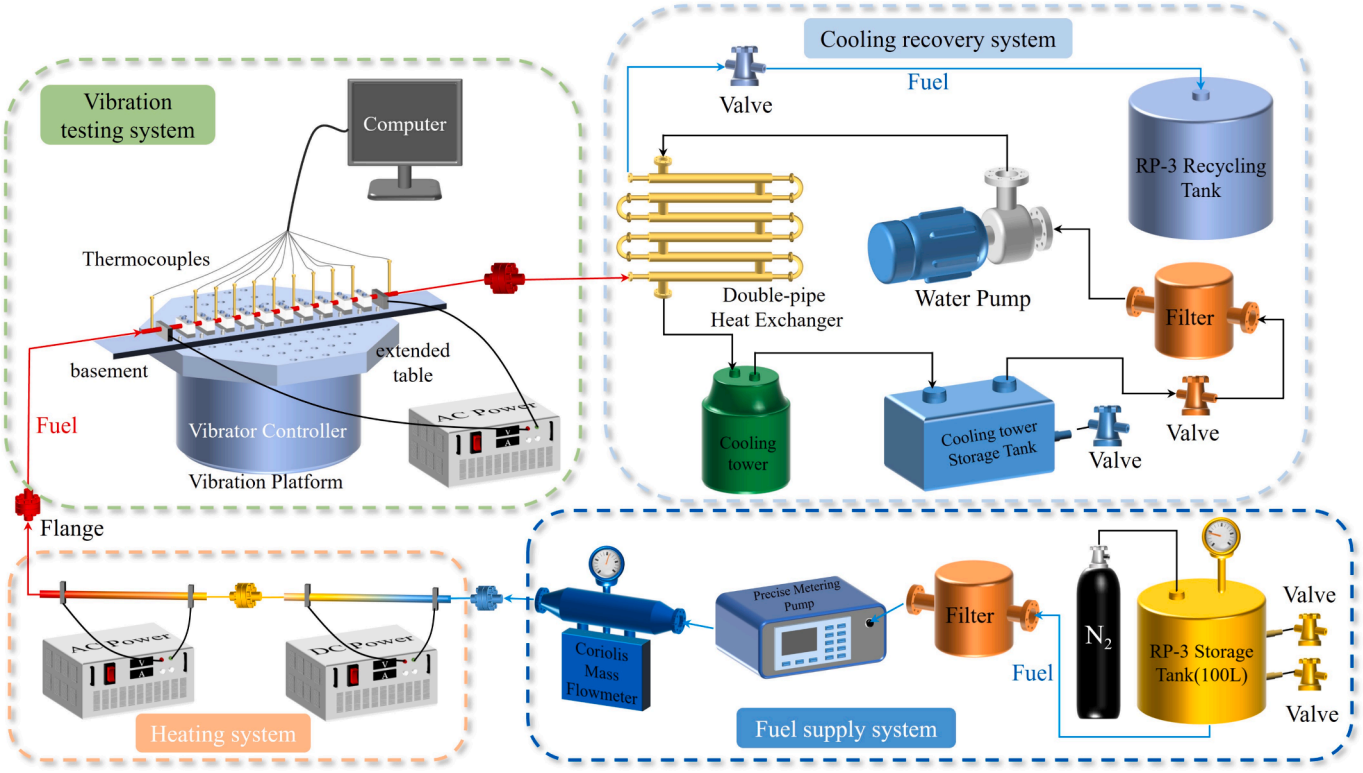

Fig. 1. Schematic of the experimental system.

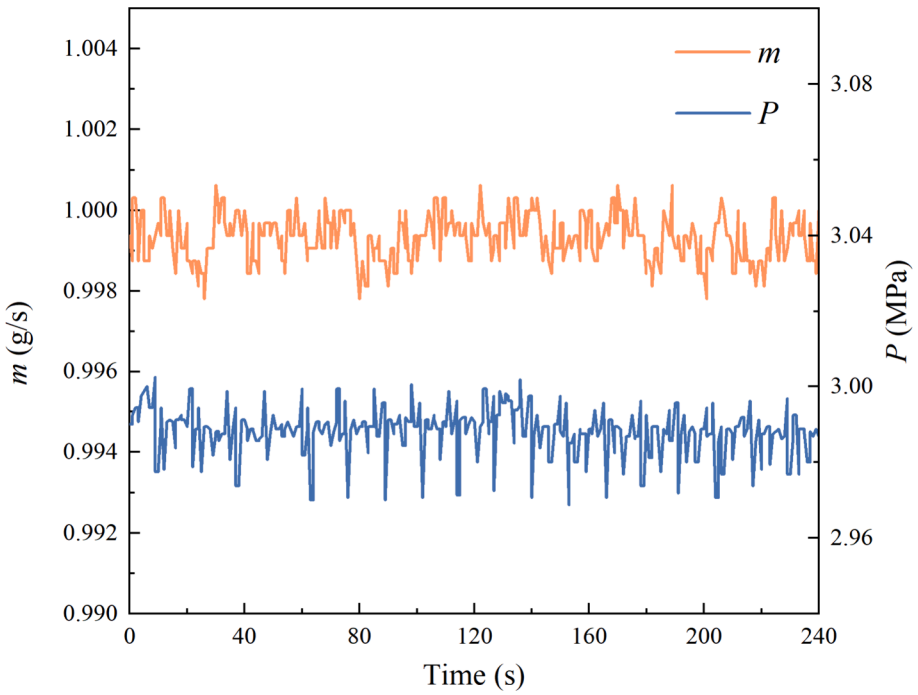

Fig. 2. Variations of mass flow rate and pressure of the experimental system with time.

temperatures, a two-stage heating system is installed prior to the test section, which is heated by a 30 kW DC (direct current) and 380 V industrial AC (alternating current) voltage-stabilized power supply. Insulating flanges are installed at the connections before, between, and after the two-stage preheating sections to prevent electrical leakage. The insulating gaskets before and after the first preheating section are made from polytetrafluoroethylene (PTFE), which can operate long-term at temperatures up to 200 °C; the insulating gasket after the second preheating section is made from mica, with a long-term operating temperature of 500 °C and can withstand up to 850 °C for short periods. RP-3 is heated up to a maximum of 150 °C after passing through the first stage pre-heating section, while up to 400 °C after passing through the second stage pre-heating section. For the vibration testing system, the static pressure is detected by a pressure transmitter (Rosemount 3051CA4). Two K-type I armored thermocouples with tee joints are installed to monitor the fuel temperature at both the outlet and inlet regions of the employed tube. To avoid measurement errors due to uneven mixing of the fluid inside the tube, this work uses a custom-designed tee joint for temperature measurement. Armored thermocouples are fixed to one side of the joint, and the probe length of the thermocouples is carefully designed to ensure that the tip is positioned right at the center of the fluid flow path. Additionally, near the inlet of the joint, there is a mixing chamber equipped with three layers of 200-mesh stainless steel metal mesh to facilitate even mixing of the fluid. Detailed information about the test section will be provided in Section 2.2. After following through the test section, RP-3 is cooled below 30 °C through a double-pipe heat exchanger by cooling water and subsequently directed into the recovery tank via a back-pressure valve in the cooling recovery system.

The thermal properties (density [46], isobaric specific heat capacity [47], thermal conductivity [48], and dynamic viscosity [49]) of RP-3 (P_c = 2.33 MPa) are obtained from the literature.

2.2. Test section

The test section is shown in Fig. 3. The tests were designed using a stainless steel 321 tube with an outer diameter of 2.2 mm and an inner diameter of 1.807 mm. The tube features a heated section measuring 0.535 m, an adiabatic entrance section measuring 0.15 m, and an adiabatic exit section measuring 0.115 m. The tube is installed horizontally and fixed on the substrate, where the white clamping blocks are made of zirconium dioxide (ZiO_2) ceramic to reduce the heat dissipation. The heat insulation block is made of stainless steel, and the edges in contact with the clamping block and the substrate are serrated to effectively reduce the thermal conduction. The tube and the pressure measuring joint are connected by laser welding. These components are capable of withstanding pressures exceeding 10 MPa and effectively reducing local resistance at connection points. The outer wall

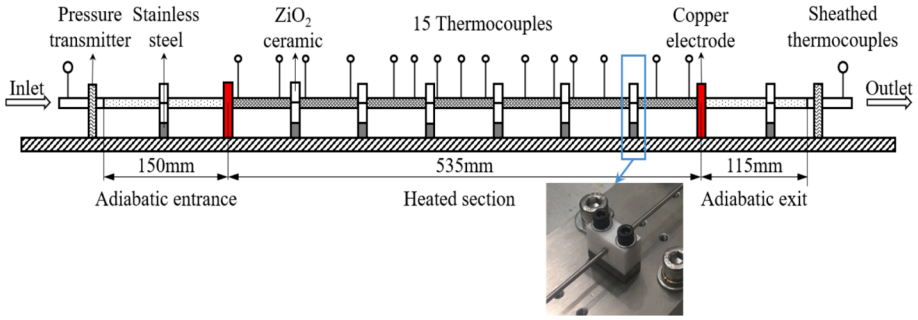

Fig. 3. Details of the test section.

temperature is monitored by fifteen K-type thermocouples, each with a wire diameter of 0.1 mm, unevenly welded onto the outer surface of the tube. All thermocouples are calibrated within the range from room temperature to 773 K. The calibration from room temperature to 573 K is conducted in a precision constant-temperature oil bath furnace, using a mercury thermometer (accuracy of 0.05 K) as the standard. The calibration from 573 K to 773 K is performed in a thermocouple calibration furnace using a Platinum10%Rhodium-Platinum (Pt10%Rh-Pt) standard thermocouple as the reference. Fig. 4 shows the calibration curve of K-type thermocouples in the experiments. To minimize the heat dissipation, the whole tube is wrapped with a layer of insulation material (Aspen), which has a thermal conductivity of 0.012 W/(m·K).

In the current work, the effect of various physical factors such as pressure, heat flux, mass flux, inlet temperature, vibration acceleration, and vibration frequency on the heat transfer performance under vibration is investigated. Table 1 lists a detailed description of the working conditions. The standard working condition for the present study is set as: system pressure of 5 MPa, inlet temperature of 298 K, the mass flux of 195 kg/(m^2·s), vibration acceleration of 5 g, and vibration frequency of 191 Hz.

2.3. Data reduction

The local HTC can be expressed as follows:

$$h_x = \frac{q_x}{T_{wx,in} - T_{b,x}} \tag{1}$$

where $T_{wx,\mathrm{in}}$ and $T_{b,x}$ stands for the temperatures of the inner wall and fuel bulk, respectively. The effective heat flux q_x is determined as Eq. (2):

$$q_x = \frac{I^2\rho(T)/\left[\pi\left(r_{out}^2 - r_{in}^2\right)\right]}{\pi d} - q_{loss,x} \tag{2}$$

where $q_{loss,x}$ represents the local heat loss, I denotes the current, $\rho(T)$ denotes the electrical resistance of the heated tube, d represents the tube diameter, r_{in} and r_{out} are the inner and outer radius of the tube, respectively.

The Re and local Nu in the tube could be expressed by

$$Re = \frac{\rho u d}{\mu} = \frac{4m}{\pi d\mu} \tag{3}$$

$$Nu_x = \frac{h_x d}{k_x} \tag{4}$$

Table 1
Experimental parameters.

Parameter	Value
Mass flux (kg/(m^2·s))	117, 195, 273
System pressure (MPa)	3, 4, 5
Heat flux (kW/m^2)	36, 60, 84, 108
Inlet temperature (K)	323, 348, 373
Vibration accelerate (m/s^2)	0–6 g
Vibration frequency (Hz)	5–80, 180–650

where m represents the mass flow rate, h represents the heat transfer coefficient, and μ and k denotes the viscosity and thermal conductivity of RP-3, respectively.

In the current study, the one-dimensional heat conduction equation in the cylindrical coordinate system [50] is used to calculate the inner wall temperature. Tube heating can be considered to be a homogeneous body heat source, and the heat differential equation is

$$\frac{1}{r}\frac{\partial}{\partial r}\left(\lambda r\frac{\partial T}{\partial r}\right) + \Phi = 0 \tag{5}$$

In Eq. (5), the internal heat source item is

$$\Phi = \frac{I^2\rho(T)}{\pi^2\left(r_{\mathrm{out}}^2 - r_{\mathrm{in}}^2\right)^2} \tag{6}$$

The boundary conditions are defined: $r = r_{out}$, $k\frac{\partial T}{\partial r} = q_{loss,x}$ and $T = T_{w,out}$.

For calculation of the inner wall surface temperature $T_{w,in}$, integrating the differential equation from r_{in} to r_{out}, Eq. (7) could be given:

$$T_{w,in} = T_{w,out} - \left[\left(\Phi\frac{r_{out}^2}{2} - q_{x,loss}(T)r_{out}\right)\ln\frac{r_{out}}{r_{in}} - \frac{\Phi}{4}\left(r_{out}^2 - r_{in}^2\right)\right]\Big/ k_x \tag{7}$$

The recorded RP-3 enthalpy-difference curve and the wall heating power could contribute to deriving the distribution of the fluid bulk temperature along the heated tube [51]. Therefore, the following inverse function could be employed to determine the local RP-3 bulk temperature.

$$T_{b,x} = H^{-1}\left[\frac{Q_x}{m} + H(T_{in})\right] \tag{8}$$

The heating power Q_x could be obtained as below:

$$Q_x = I^2\int_0^x\left(\frac{\rho(T)}{\pi\left(r_{out}^2 - r_{in}^2\right)}\right)dx - \pi d_{\mathrm{out}}\int_0^x q_{x,loss}(T)dx \tag{9}$$

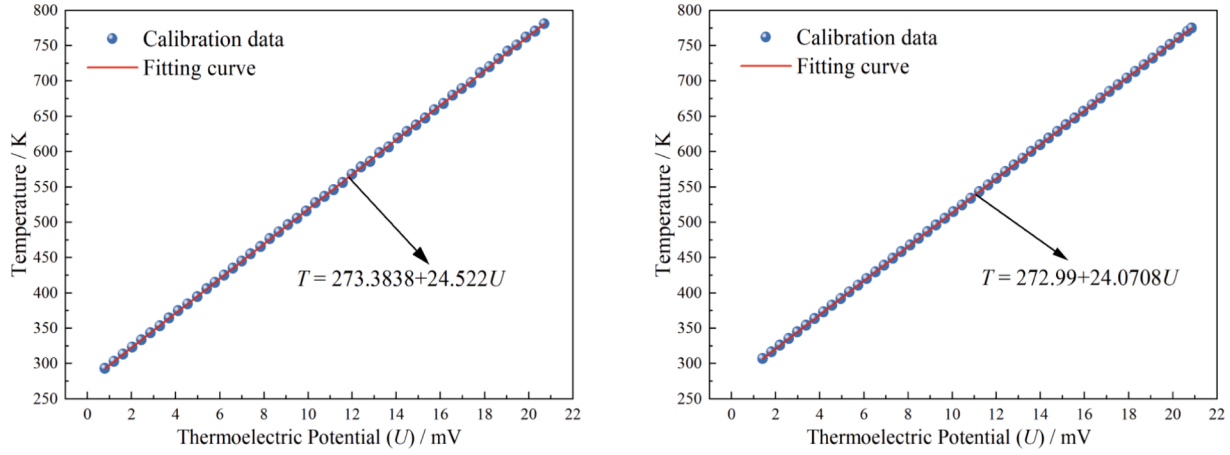

(a) K-type armored thermocouple (b) K-type wall temperature thermocouples

Fig. 4. Calibration curve of K-type thermocouples.

The buoyancy effect, which arises from the sharp change of thermal properties, is particularly essential in horizontal flows. There are many criterion numbers [52–55] used to assess the impact of buoyancy, among them, Petukhov et al. [56] introduced the dimensionless parameters Gr_q and Gr_{th} to assess the influence of the buoyancy in a horizontal tube, which is similar to the current experimental situation:

$$Gr_q = \frac{g\overline{\alpha}q''d^4}{\nu_b^2 k_b} \tag{10}$$

$$Gr_{th} = 3\times10^{-5}Re_b^{2.75}\overline{Pr}^{0.5}\left[1+2.4Re_b^{-1/8}\left(\overline{Pr}^{2/3}-1\right)\right] \tag{11}$$

where,

$$\overline{Pr} = \frac{i_w - i_b}{T_w - T_b}\frac{\mu_b}{k_b} \tag{12}$$

$$\overline{\alpha} = \frac{1}{\rho_{film}}\frac{\rho_b - \rho_w}{T_w - T_b} \tag{13}$$

and i stands for the enthalpy. The subscript "w" represents the average temperature of upper and lower surfaces, and "b" is the fuel bulk temperature.

2.4. Uncertainty analysis

The experimental uncertainties of direct measurements are displayed in Table 2. The application of the error propagation formula [57] allows for the calculation of the uncertainty in the effective heat flux of the tube wall, as follows:

$$\left|\frac{\Delta q_x}{q_x}\right| = \sqrt{\left(\frac{q_x+q_{loss}}{q_x}\right)^2\varepsilon^2(q_{0,x}) + \left(\frac{q_{loss,x}}{q_x}\right)^2\varepsilon^2(q_{loss,x})} = 2.7\% \tag{14}$$

The uncertainties of total heat flux and heat loss are given by

$$\left|\frac{\Delta q_{0,x}}{q_{0,x}}\right| = \sqrt{4\varepsilon^2(I) + \left(\frac{2d_{out}^2}{d_{out}^2-d_{in}^2}\right)^2\varepsilon^2(d_{out}) + \left(\frac{2d_{in}^2}{d_{out}^2-d_{in}^2}\right)^2\varepsilon^2(d_{in}) + \varepsilon^2(d_{out})} = 2.58\% \tag{15}$$

$$\left|\frac{\Delta q_{loss,x}}{q_{loss,x}}\right| = \sqrt{\varepsilon^2(I)+\varepsilon^2(U)+\varepsilon^2(d_{out})+\varepsilon^2(L)+\varepsilon^2(T_{wx,out})} = 0.85\% \tag{16}$$

The temperature difference between the fluid bulk and the inner wall is consistently above 32 K in all experimental conditions. Therefore, the uncertainty is estimated by the following equation:

$$\left|\frac{\delta(\Delta T)}{\Delta T}\right| = \frac{\sqrt{|\delta T_{wx,in}|^2 + |\delta T_{bx}|^2}}{32} = 4.2\% \tag{17}$$

in which the uncertainty of inner wall temperature $\delta T_{wx,in}$ is 1.05 K and the local fluid bulk temperature δT_{bx} carries an uncertainty of 0.85 K.

Hence, the uncertainty of local HTC is written as follows:

Table 2
Experimental uncertainties of direct measurements.

Measured parameters	Instruments	Precisions
Outer wall temperature (K)	K-type thermocouple	±0.3–1 K
Fuel temperature (K)	K-type armored thermocouple	±0.6–0.8 K
Mass flow rate (kg/s)	Coriolis mass flow meter	±0.15 %-0.3 %
Voltage (V)	Voltmeter with export	±0.2 %
Current (A)	Ampere meter with export	±0.2 %

$$\left|\frac{\Delta h_x}{h_x}\right| = \sqrt{\varepsilon^2(q_x)+\varepsilon^2(\Delta T)} = 4.99\% \tag{18}$$

The uncertainty of the thermal conductivity is less than 3 % based on the measurement data [51]. Thus, the uncertainty of the Nu could be calculated:

$$\left|\frac{\Delta Nu_x}{Nu_x}\right| = \sqrt{\varepsilon^2(h_x)+\varepsilon^2(k)} = 5.82\% \tag{19}$$

2.5. Vibration reliability verification of test bench

When the excitation frequency of a force is close to the natural frequency of an object, resonance occurs. In this experiment, resonance could cause severe damage to the experimental pipes or the test bench, making it essential to determine the resonant frequencies of these components. To ensure safety, the experimental conditions should avoid these frequencies. While resonance can occur at various frequencies, the first-order resonance has the most significant impact on the structure, thus receiving the most attention.

The vibration platform provides a vibration frequency in the range of 5 Hz to 4000 Hz, a maximum acceleration of 1000 m/s^2 with an unloaded capacity of 70 kg. According to the vibration platform documentation, the first-order resonant frequency of the vibration platform is above 4000 Hz, and the first-order resonance frequency of the extended table is above 2000 Hz, both of which are significantly higher than the experimental conditions, thus do not need to be considered. The substrate is analyzed using ABAQUS software [58]. The results reveal that the resonant frequency of the substrate is 133 Hz. Under a vibration acceleration of 6 g, the displacement of the substrate endpoints as a function of vibration frequency is illustrated in Fig. 5(a). It shows that the maximum amplitude at the endpoint of the substrate is less than 0.5 mm within the scope of 5–110 Hz and 153–4000 Hz. At lower vibration accelerations and away from the endpoints, the amplitude is even smaller, hence these frequency ranges can be considered safe frequencies. Furthermore, computational results indicate that under safe frequencies, the maximum principal stress on the substrate is 79.4 MPa, and the maximum shear stress is 14.02 MPa, both of which are significantly lower than the yield stress of the substrate made by 316L stainless steel (170 MPa). Based on these findings, the vibration platform and substrate can be safely used in non-continuous experiments at these frequencies without risk of structural failure.

When a stainless steel tube is fixed to the substrate as previously described, each segment of the tube between two adjacent fixed points can be considered as a beam fixed at both ends, which is analogous to a simply supported beam connected to two cantilever beams. The mechanical model can be described by the Euler-Bernoulli beam theory [59]. Due to the stainless steel tube involved in this study having a high length-to-diameter ratio ($L/d \approx 243$) and relatively thin wall, it exhibits low rigidity. If the span between fixed points is too large, significant deformation can occur in the middle part of the tube under vibrational excitation. This would result in changes in vibration acceleration along the fluid flow direction, introducing additional variables that are not conducive to controlled variable studies. Therefore, it is necessary to calculate the appropriate distance between adjacent fixed points to ensure that the amplitude at any point on the tube does not become excessive under experimental conditions.

Using ABAQUS software to analyze the vibration characteristics of the tube, the simulation assumes that the fluid inside the tube is distributed evenly along its mass. The results indicate that with adjacent fixed points at distances of 50 mm, 75 mm, and 100 mm, the corresponding first-order resonant frequencies are 5078.9 Hz, 2257.3 Hz, and 1300.4 Hz, respectively. Moreover, Fig. 5(b) shows the amplitude variations in the middle of the tube under an acceleration of 6 g across frequencies. It is observed that the maximum amplitude in the middle of the tube is less than 0.01 mm at the resonant frequency, and less than

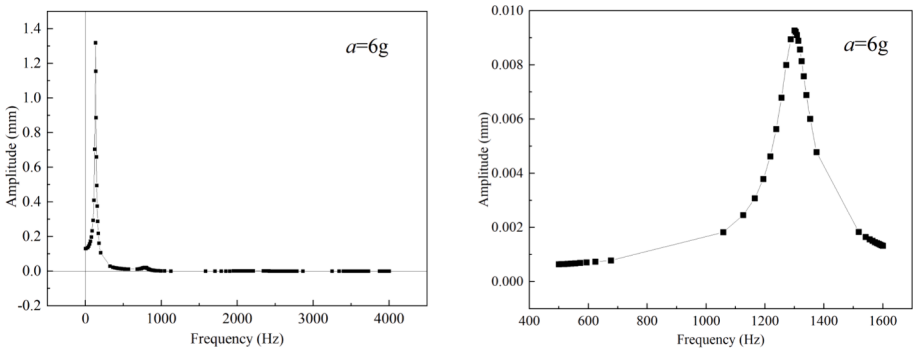

(a) at the endpoint of the substrate (b) in the middle of the tube

Fig. 5. Amplitude changing with frequencies.

0.002 mm in the range below 1000 Hz. Based on these findings, an adjacent fixation point distance of 100 mm is chosen for the experiments.

Based on the analysis above, within the frequency ranges of 5–110 Hz and 153–1000 Hz, the structure of the test bench is safe. Additionally, when the distance between adjacent fixed points on the experimental tube is set at 100 mm, the tube can vibrate along with the test bench without inducing any additional string vibrations.

3. Results and discussion

This section details experimental research into the convective heat transfer characteristics of supercritical pressure aviation kerosene RP-3 in a tubular laminar flow, examining how vibrations affect its heat transfer performance under varying conditions. It specifically focuses on how the system pressure (3–5 MPa), heat flux (36–108 kW/m^2), mass flux (117–273 kg/m^2/s), inlet temperature (323–373 K), vibration acceleration (0–6 g), and vibration frequency (5–650 Hz) enhance the heat transfer characteristics.

3.1. Effect of system pressure

The fluctuations of the inner wall temperature and HTC in the laminar regime for various system pressures of 3, 4, and 5 MPa are plotted in Fig. 6(a) and (b). At the $Re_i = 440$, the inner wall temperature rises progressively and the pressure plays a less role in the wall temperature distribution. At the outlet, the fuel bulk temperature has reached above 480 K with *Re* of 2000. This indicates that as the Reynolds number and the bulk temperature of RP-3 increase along the flow path, its flow develops towards the transition regime, and the influence of the thermal properties gradually becomes more pronounced. Consequently, the impact of the pressure will become more evident in the outlet region. At high system pressures, the inner wall surface temperature increases marginally, while the HTC decreases slightly. This occurs because an increase in pressure reduces both the isobaric specific heat capacity and the Prandtl number for RP-3. Hence, under consistent heating power, these changes could result in an increased bulk temperature of RP-3, a decreased HTC, and a rising wall temperature at the same axial position.

During the current test, when the tube vibrated at a frequency of 191 Hz and an acceleration of 5 g, the heat transfer enhancement was observed across all system pressures, albeit to varying extents. Fig. 6(c) demonstrates the heat transfer enhancement ratio (HTER, defined as the ratio of HTC with vibration to that without) variations at different system pressures of 3, 4, and 5 MPa. It presents that the initial region (dimensionless position $x/d < 75$, $Re < 680$) has less enhancement effect. The closer to the outlet region brings the higher *Re*, resulting in a stronger enhancement effect of the vibration. This is attributed to the relatively long entrance region of laminar flow, where the heat transfer depends on the momentum exchange between layers, leading to the limited influence of the vibration on turbulence and mixing enhancement. The maximum value of the HTER reaches 1.8 at the dimensionless location $x/d = 250$. As the laminar flow approaches the outlet region, the transition starts, which contributes positively to the heat transfer enhancement at the non-vibration state and lowers the HTER. In addition, by comparing the curves of different pressures in Fig. 6(c), it is obviously observed that the HTER hardly changes with system pressures ranging from 3 MPa to 5 MPa, exhibiting a maximum relative deviation of only 3.9 % at different pressures. While at higher *Re* in laminar flow, the higher system pressure contributes to lower HTER. The "reversal" of HTER at the outlet region is also owing to the flow transition.

3.2. Effect of heat flux

According to Fig. 7(a) and (b), for the case without vibration, it is observed that the wall temperatures gradually increase along the flow path under four various heat fluxes (36, 60, 84, 108 kW/m^2), while the HTC gradually decreases. As the thermal and momentum boundary layer develops along the tube, the mainstream core area continuously shrinks. Simultaneously, the thermal boundary layer close to the wall thickens, and the temperature gradient slowly decreases. This will lead to the decreased heat transfer performance and increased wall temperature. It can also be found that when the heat flux is 84 kW/m^2 and 108 kW/m^2, the wall temperature near the outlet region drops, while the HTC increases. For the case of $q = 108$ kW/m^2, as the *Re* near the outlet region has exceeded 2300, the flow enters the transition state as depicted in Fig. 7(c). Thus, the heat transfer is enhanced, resulting in a decrease in wall temperature. While for $q = 84$ kW/m^2, the temperature near the inner wall has reached approximately 650 K, approaching the pseudo-critical point of RP-3. The isobaric specific heat capacity reaches its peak value and the heat absorption of fuel increases, resulting in heat transfer enhancement.

Under vibration conditions, the inner wall surface temperature drops by 100 K. As the heat flux increased from 36 kW/m^2 to 108 kW/m^2, the HTC improved significantly. At $q = 108$ kW/m^2, the average HTC increased by up to 36.4 %, indicating a strong dependency of the heat transfer enhancement on heat flux. Compared to the no-vibration condition, the maximum heat transfer enhancement ratios for cases with heat fluxes of 36, 60, 84, and 108 kW/m^2 are 1.72, 2.13, 1.78, and 1.99, respectively. It can also be concluded that the vibration could speed up the transition from laminar flow to turbulent flow. As depicted in Fig. 7 (a), a comparison of wall temperatures between vibration and non-vibration states under the standard working condition described in Section 2.2 reveals that the higher heat fluxes precipitate an earlier separation of temperatures. This suggests that the axial position at which vibration begins to enhance the heat transfer is correspondingly earlier. For example, at a heat flux of 36 kW/m^2, the enhancement of the heat transfer is notably initiated at a farther position along the tube (at $x/d =$ 196), whereas at a heat flux of 108 kW/m^2, the enhancement occurs

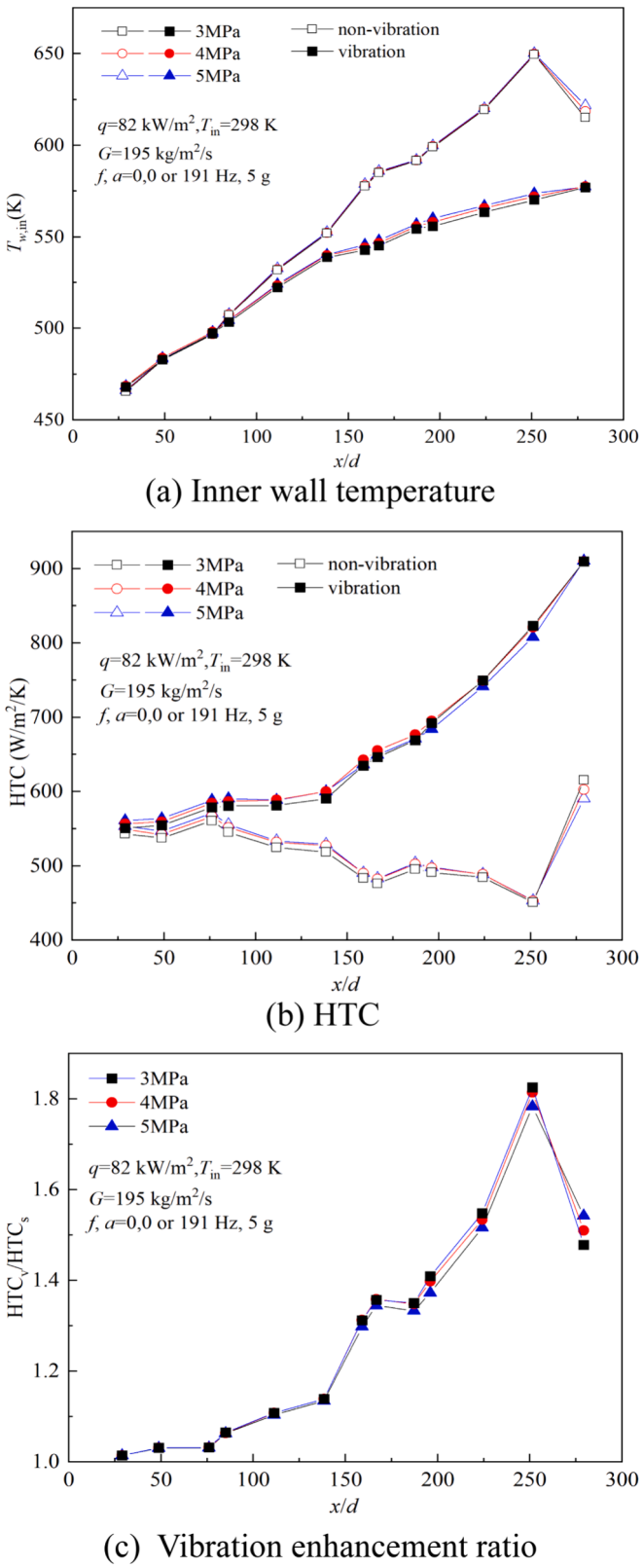

Fig. 6. Vibration effects on heat transfer under various system pressures of 3, 4, and 5 MPa.

closer to the front (at x/d = 85). Fig. 7(d) shows the vibration enhancement ratio variations at heat fluxes of 36, 60, 84, and 108 kW/m^2. Taking the vibration enhancement ratio of 1.05 as the reference, for q = 36, 60, 84, and 108 kW/m^2, the dimensionless axial position x/d where the enhancement ratio equals 1.05 are 152.4, 110.9, 75 and 54.8, respectively. This indicates that the higher the heat flux, the earlier the axial position where vibration begins to enhance heat transfer. This phenomenon could be attributed to the combined effects of the *Re* and buoyancy. When the flow remains in the laminar regime, the increasing *Re* could enhance the vibration enhancement effect. However, the increase in heat flux also increases buoyancy force, and the increase in buoyancy weakens the vibration enhancement effect. That is to say, *Re* and buoyancy have opposing effects on the vibration enhancement effect. In this process, the effect of the increasing *Re* is dominant, therefore, the final result is that the HTER increases with the increase of the heat flux. In addition, it can be found that the vibration enhancement effect is weakened near the outlet region when the heat flux exceeds 84 kW/m^2, as demonstrated in Fig. 7(d). It is attributed to the fact that *Re* near the outlet region has already exceeded the transition point. The mixing effect in the radial direction of the turbulence weakens the vibration enhancement effect, making the effect of vibration less significant.

In the above process, consideration must be given to the effects of the buoyancy and thermal acceleration on the heat transfer enhancement. Discussions primarily focus on the non-dimensional parameters Gr_q/Gr_{th} [56] and Kv [60]. It is generally considered that the impacts of the buoyancy and thermal acceleration could be ignored when $Gr_q/Gr_{th} < 1$ and $Kv < 3 \times 10^{-6}$, respectively. For laminar flow, due to the large temperature difference between the wall temperature and RP-3 bulk temperature, the buoyancy force has a significant influence, with the maximum Gr_q/Gr_{th} reaching 22.2.

As depicted in Fig. 8(a), the ratios of Gr_q/Gr_{th} along the heated tube are all larger than 1 under four different heat fluxes, both in vibration and non-vibration states. The maximum Gr_q/Gr_{th} reaches 22.2 at x/d = 251.3, and the minimum Gr_q/Gr_{th} reaches 2.4 at x/d = 28.8. When the dimensionless length $x/d < 150$, the ratio of Gr_q/Gr_{th} with vibration is slightly higher than that without. Moreover, the increase in Gr_q/Gr_{th} with vibration is more pronounced in cases of higher heat flux ($q \geq 84$ kW/m^2), suggesting that vibration contributes positively to enhancing the buoyancy effects in the entrance region. This occurs since, when the dimensionless length $x/d < 150$, the *Re* remains relatively low and the development of the thermal boundary layer is incomplete. Consequently, vibration inhibits the increase of the turbulent kinetic energy and then enhances the buoyancy. When the dimensionless location $x/d \geq 150$, the ratios of Gr_q/Gr_{th} decrease when subjected to vibration, indicating that the vibration reduces the impact of the buoyancy. At high heat flux (q = 108 kW/m^2) and near the outlet region ($x/d > 196$), vibration can weaken the effect of the buoyancy, resulting in at least an 18.3 % decrease in Gr_q/Gr_{th}. It is attributed to the fact that the vibration strengthens the mixing of the mainstream and fluid close to the wall, reducing the difference in temperature between the wall and the mainstream, and weakening the buoyancy effect correspondingly. Compared with the wall temperature distribution shown in Fig. 7(a), this analysis aligns with the observed pattern of wall temperature distribution. The values of the thermal acceleration factor Kv are all below 3×10^{-6} as illustrated in Fig. 8(b). Therefore, although the Kv rises slightly by vibration, it can still be considered that the influence of the thermal acceleration is minimal and could be ignored.

3.3. Effect of mass flux

Fig. 9(a) and (b) demonstrate the variations of the inner wall temperature, fuel bulk temperature, and HTC changes versus the dimensionless length x/d of the tube at three different mass fluxes of 117, 195, and 273 kg/(m^2·s), with the inlet *Re* ranging from 209 to 507, and outlet *Re* from 1369 to 1415.

For the case without vibration, the results exhibit the same characteristics as those described in the previous section, namely, the wall temperatures gradually increase along the flow path while the HTC gradually decreases. Due to the low *Re* along the tube, the heat transfer

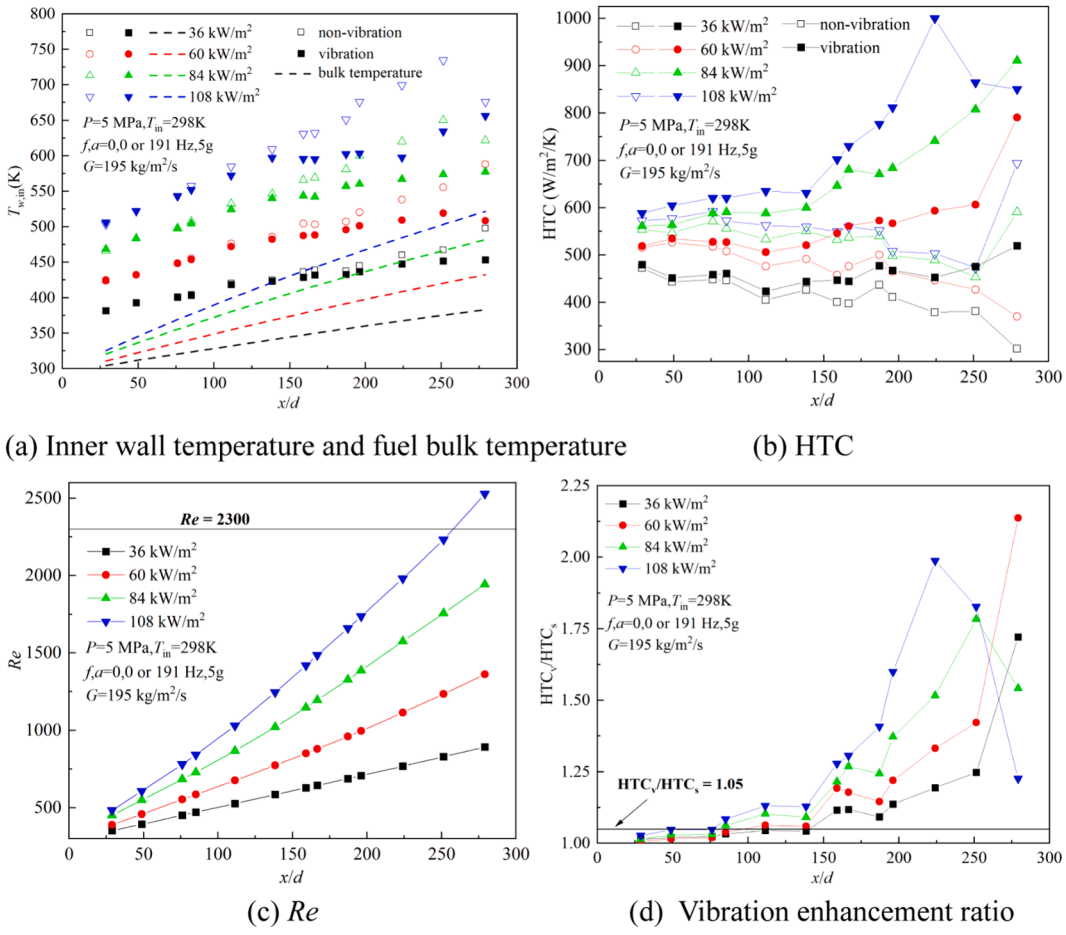

Fig. 7. Vibration effects on heat transfer under four different heat fluxes of 36, 60, 84, and 108 kW/m^2.

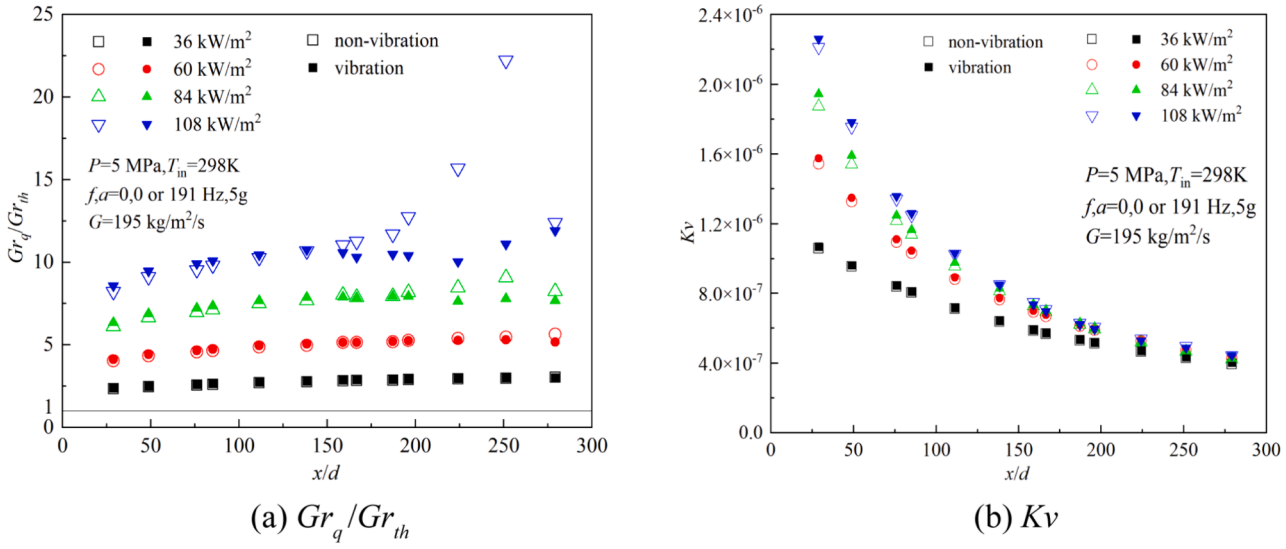

Fig. 8. Gr_q/Gr_{th} and Kv variations under four different heat fluxes of 36, 60, 84, and 108 kW/m^2.

is greatly affected by the entrance effect, causing a slight decrease in the HTC. In contrast, under vibration conditions, the HTCs gradually increase along the flow path for all three mass fluxes, and there is a significant increase in the HTC in the outlet region. For example, in the outlet region at $x/d = 279.1$, under three different mass fluxes of 117, 195, and 273 kg/(m^2·s), the HTER reaches its maximum values of 2.02, 2.14, and 1.86, respectively. With the mass flux increasing, the HTER reduces as a result of the combined effects of growing *Re* and buoyancy, as observed in Fig. 9(c). For the laminar regime, the increase in *Re* could strengthen the vibration-enhanced heat transfer effect, whereas the increase in buoyancy could weaken the enhancement caused by vibration. However, the buoyancy effect takes a dominant role in this process, thus,

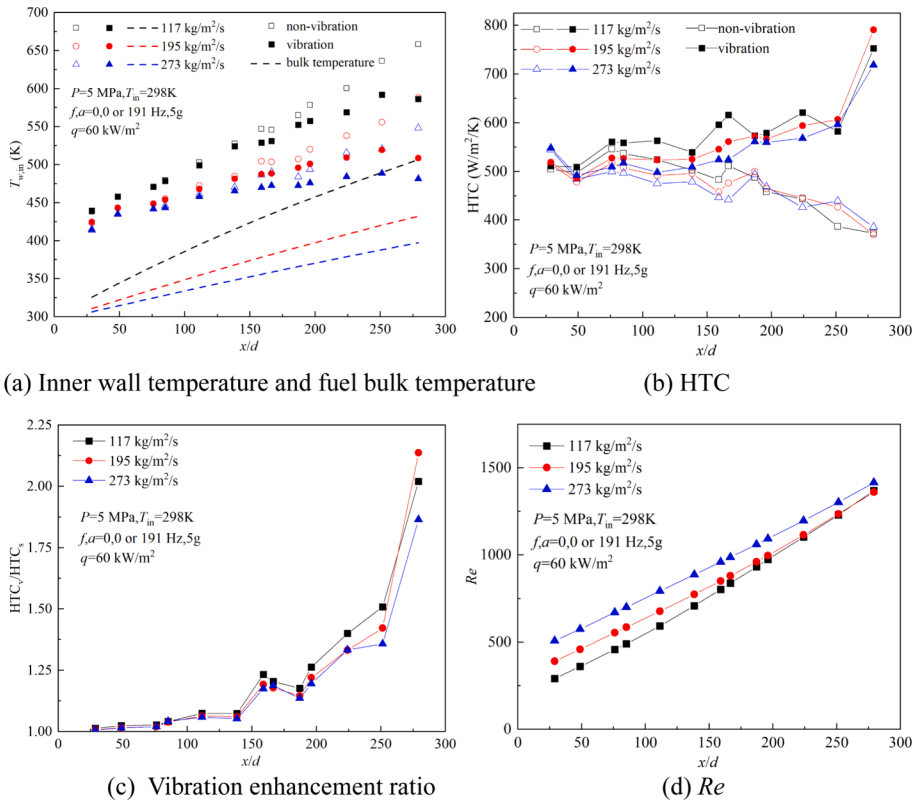

Fig. 9. Vibration effects on heat transfer at three different mass fluxes of 117, 195, 273 kg/(m^2·s).

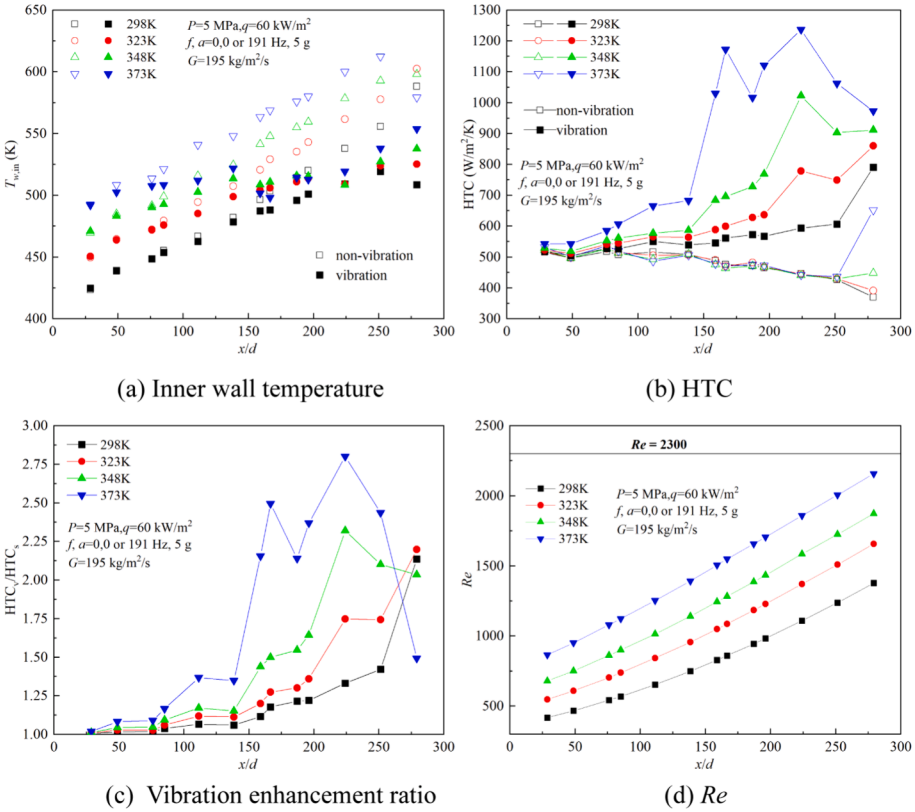

Fig. 10. Vibration effects on heat transfer at four different fuel inlet temperatures of 298, 323, 348, and 373 K.

Fig. 9(c) shows that the HTER decreases with the increase in mass flux. Especially, HTER in the case of G=195 kg/(m^2·s) exceeds that in the case of G=117 kg/(m^2·s) at x/d = 279.1. It could be explained that the local *Re* for G=117 kg/(m^2·s) has a larger value than that for G=195 kg/(m^2·s), as presented in Fig. 9(d).

3.4. Effect of inlet temperature

The inner wall temperature and HTC variations along the tube at four different fuel inlet temperatures, i.e. 298, 323, 348, 373 K, are depicted in Fig. 10(a) and (b), respectively. In the experiments, the inlet *Re* varied from 418 to 895, and the outlet *Re* varies in the range of 1378 to 2158, as shown in Fig. 10(d). For the case without vibration, it is obvious that the wall temperature rises progressively and the HTC decreases along the tube. At x/d < 138.4, the HTCs are almost identical at various inlet temperatures, which is approximately 510.3 W/(m·K). This is because, in the non-outlet sections, the *Re* is lower and the heat fluxes are maintained the same, which affects the HTC in an equate manner. However, in scenarios with high inlet temperatures (T_{in} > 348 K), the outlet wall temperature drops due to the large *Re* at the outlet and the flow transition. Hence, combining Eq. (1), it can be inferred that under high inlet temperatures (T_{in} > 348 K), the HTC in the outlet region will significantly increase, as shown in Fig. 10(b). When the tube vibrates, the heat transfer along the path is enhanced ranging from 1.02 to 2.8 times at $x/d \geq 28.8$ for all inlet temperatures. As illustrated in Fig. 10(c), the heat transfer enhancement improves with growing inlet temperature owing to the larger local *Re* under high inlet temperature, and the highest HTER observed in all data is 2.8, occurring at x/d = 224.1 with the inlet temperature of 373 K. Near the outlet region, the HTER under four different inlet temperatures rises sharply. For the inlet temperatures of 323 K, 348 K, and 373 K, the peak vibration enhancement ratios are 2.20, 2.32, and 2.49 respectively, and the corresponding dimensionless peak locations are x/d = 279.1, 224.1, and 166.7. It indicates that as the inlet temperature increases, the vibration enhancement ratio at the peak also rises, and the peak position occurs earlier. This result is similar to the phenomenon observed with the effect of the heat flux and is also a result of the combined effect of buoyancy and *Re*. Different from the experimental results described in Section 3.2, the HTER presents a double peak at a higher inlet temperature. It results from the unsynchronized effect of the buoyancy and *Re*. At the inlet temperature of 373 K, a higher peak would typically be expected. However, since the buoyancy weakens the enhancement effect of vibration, the expected single peak disappears and develops into two sub-peaks.

3.5. Effect of vibration acceleration

Fig. 11(a) and (b) present the variations of the inner wall temperature and HTC under thirteen different vibration accelerations (0–6 g, with intervals of 0.5 g). It can be seen that the inner wall temperature decreases monotonously with the increase of the vibration acceleration, while HTC enhances correspondingly. Fig. 11(c) describes the vibration enhancement ratio variations under twelve different vibration accelerations (0.5–6 g, with intervals of 0.5 g). Near the inlet region, the vibration accelerations have little impact on the HTER. Specifically, as the vibration acceleration increases from 0.5 g to 6 g, at x/d = 28.81, the HTER remains constant at 1. Meanwhile, at x/d = 76.06, HTER varies within the range of 1 to 1.01. In contrast, the closer to the outlet region, the greater the impact of the vibration acceleration on the vibration enhancement ratio. For instance, the HTER varies in the range of 1.01 to 1.17 at x/d = 279.14 with vibration acceleration increasing from 0.5 g to 6 g. Detailed analysis can be conducted by integrating the experimental data. At x/d = 28.81, the wall temperature difference between the vibration acceleration of 0 g (non-vibration state) and 6 g is only 2.15 K, and the HTC only rises by 0.44 %. However, at x/d = 279.14, the maximum difference in wall temperature is 28.13 K, and HTC increases by 17.4 %. This is due to the higher *Re* near the outlet, where the

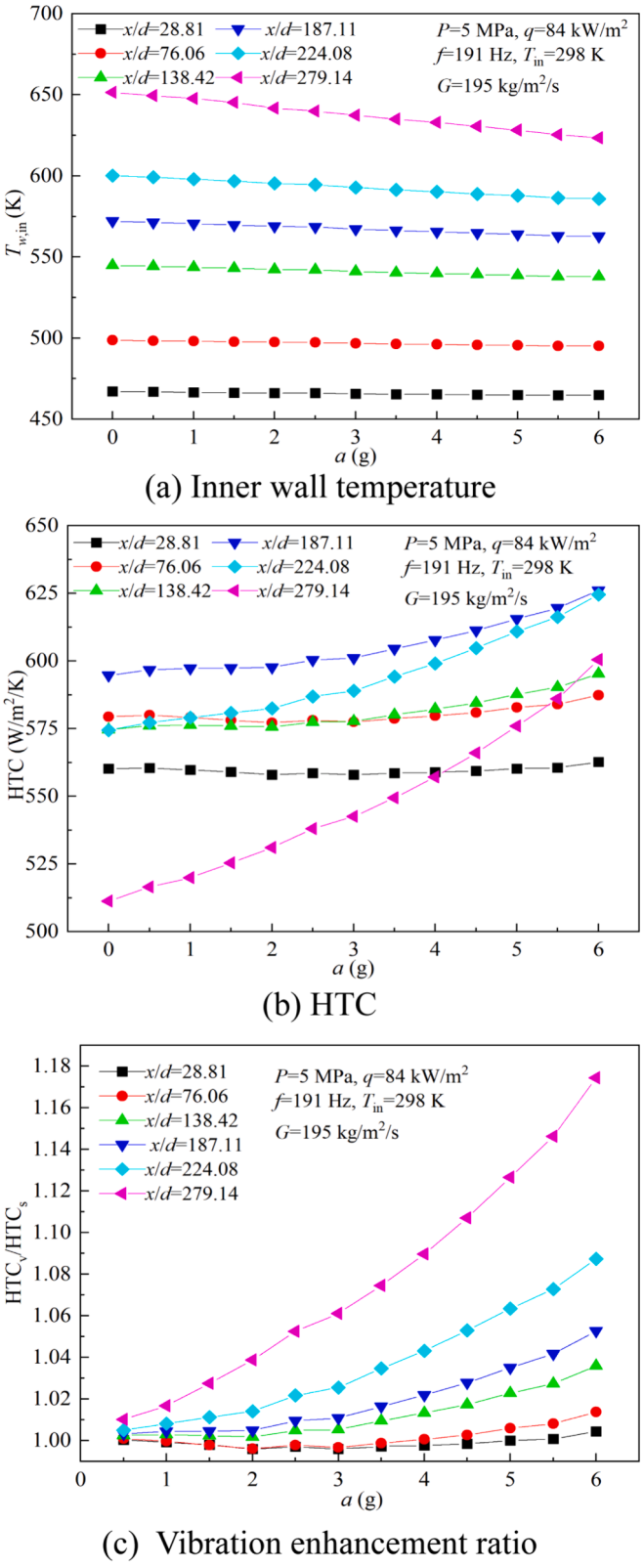

Fig. 11. Response of different parameters under thirteen different vibration accelerations (0–6 g, with intervals of 0.5 g).

vibration has a more pronounced enhancing effect on the heat transfer. It indicates that the HTER improves with the increase of the vibration acceleration, and similarly, the growth rate of the HTER. At the same dimensionless position x/d, the higher vibration acceleration leads to

the faster growth of the HTER. This phenomenon can be attributed to the fact that, with an increase in the vibration acceleration, both the enhancement of vibration's impact on the heat transfer and the inhibitory effect of the vibration on the buoyancy become more pronounced. As a result, the influence of the buoyancy on the heat transfer deterioration is diminished.

3.6. Effect of vibration frequency

In aero engines, the primary sources of vibration are the combustion chamber and the main shaft, with heat exchangers often installed on the combustion chamber's exterior casing. Consequently, vibrations from the combustion chamber substantially influence heat transfer. This study's selection of vibration frequencies is primarily influenced by the operational conditions of the combustion chamber. Literature data indicate that Solar Turbines' gas turbine combustion chambers typically operate at vibration frequencies between 315–370 Hz and 440 Hz [61]. GE's aero engines exhibit vibration frequencies ranging from below 30 Hz to between 100–1000 Hz [62], while Siemens' gas turbines primarily operate at frequencies of 50–300 Hz, 420 Hz, and 566 Hz [63]. Overall, these frequencies are mostly below 650 Hz. Given the safe frequencies verified for vibration reliability in Section 2.5 and the experimental capabilities of our system, the chosen vibration frequencies for this study's experiments were set within the range of 20–80 Hz and 180–650 Hz.

The average inner wall temperature fluctuates in the vibration frequency ranges of 20–80 Hz and 180–650 Hz are shown in Fig. 12. The resonance frequency of the experimental substrate is 133 Hz, and for safety reasons of the experimental platform, vibration frequencies within the range of 80–180 Hz are not covered in the current experiment. The horizontal line represents the average inner wall temperature at the non-vibration state, which is 554.6 K, used as a reference for other frequencies. Vibration enhances the heat transfer at most frequencies, whereas has a detrimental effect near three frequencies: 55 Hz, 445 Hz, and 604 Hz, and the enhancement or deterioration of the heat transfer does not show a clear pattern with increasing frequency. Moreover, the strengthening or worsening of the heat transfer shows peaks in some specific frequency ranges. The heat transfer enhancement effect can be approximately separated into seven peaks: 38 Hz, 76 Hz, 191 Hz, 242 Hz, 453 Hz, 552 Hz, and 625 Hz. Among them, at frequencies of 192 Hz, 242 Hz, and 625 Hz, the average wall temperature changes are significant, and the heat transfer enhancement is pronounced.

Fig. 13 presents the inner wall temperature, HTC, and vibration enhancement ratio variations with vibrate frequencies ranges of 20–80 Hz and 180–650 Hz at six different dimensionless positions (x/d = 28.81, 85.06, 138.42, 187.11, 224.08, and 251.33), and the dashed line indicates the folded frequency range with no apparent effects. In general, as the axial location becomes closer to the outlet region, the heat transfer enhancement increases. Under all experimental vibration frequencies, the average HTER at x/d = 251.33 is 1.11 times higher than that at x/d = 28.81. However, there are some exceptions at specific locations in a few frequency ranges. For example, in the frequency range of 540–560 Hz, the wall temperature hardly changes with vibration frequency at the location of x/d = 224.08. The HTER reaches up to 1.74 at positions x/d = 251.33 at 625 Hz, and other relatively minor HTER peaks include at frequencies of 191 Hz and 242 Hz. Fig. 13(b) shows that while HTC at six different dimensionless positions (x/d = 28.81, 85.06, 138.42, 187.11, 224.08, and 251.33) varies at the same frequency, the frequency that produces the HTC peak remains consistent. This suggests that the frequency influencing the heat transfer enhancement is not significantly related to the *Re*. However, the magnitude of enhancement is affected by the local *Re*, with higher values leading to a greater vibration enhancement ratio.

The amplitudes corresponding to the three major peak frequencies (625 Hz, 191 Hz, and 242 Hz) are 0.0032 mm, 0.034 mm, and 0.021 mm, respectively. Based on calculations using the Blasius solution, the boundary layer thickness ranges from 0.7 mm to 1.56 mm under the experimental conditions listed in Table 1, influenced by *Re*. Since the amplitudes are substantially smaller at each peak frequency than the thickness of each boundary layer, the influence of the amplitudes is restricted to the boundary layer. If the impact of the vibration frequency on the heat transfer is achieved through changes in amplitude, then the heat transfer characteristics should exhibit a monotonous trend with frequency. However, from the current experimental results, it is obvious that such monotonicity is not observed. Consequently, the variation in heat transfer characteristics is likely unrelated to amplitude. In summary, the influence of the vibration frequency on enhancing heat transfer is likely associated with the dynamics of fluid–solid coupling. The stainless-steel tube's inherent frequency is altered by the presence of fuel, which accordingly changes the vibration characteristics under specific frequency excitation.

4. Empirical correlations fitting

Sieder-Tade formula [64] is a widely employed empirical correlation for *Nu* calculation of tubular laminar flow, applicable under a broad range of conditions. However, it is mainly applicable to the condition of uniform wall temperature [65], and the influence of the buoyancy is not considered enough, therefore it is not suitable to directly use as the basis for the calculation of HTC under non-vibration conditions.

Eq. (20) gives an empirical correlation for supercritical pressure RP-3 in laminar flow, which is fitted using the multiple linear regression method based on non-vibration experimental data. This correlation is in the form of the Dittus-Boelter equation [66], taking into account variations in thermal properties.

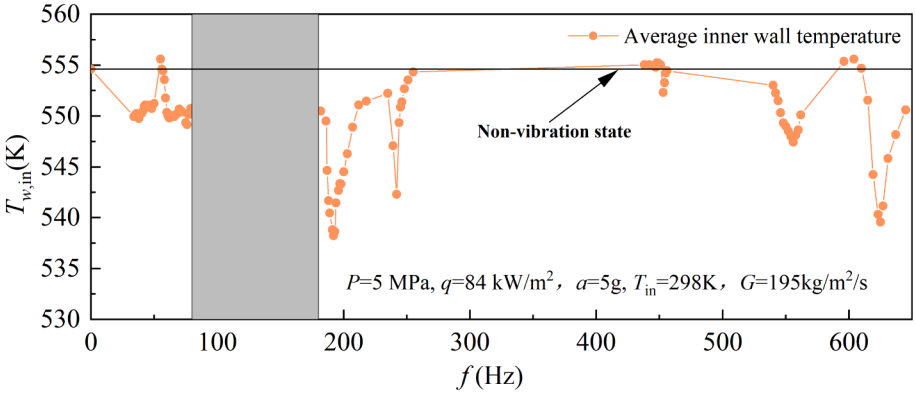

Fig. 12. Average inner wall temperature changes under different vibration frequency ranges of 20–80 Hz and 180–650 Hz (The grey area is not covered in the experiment).

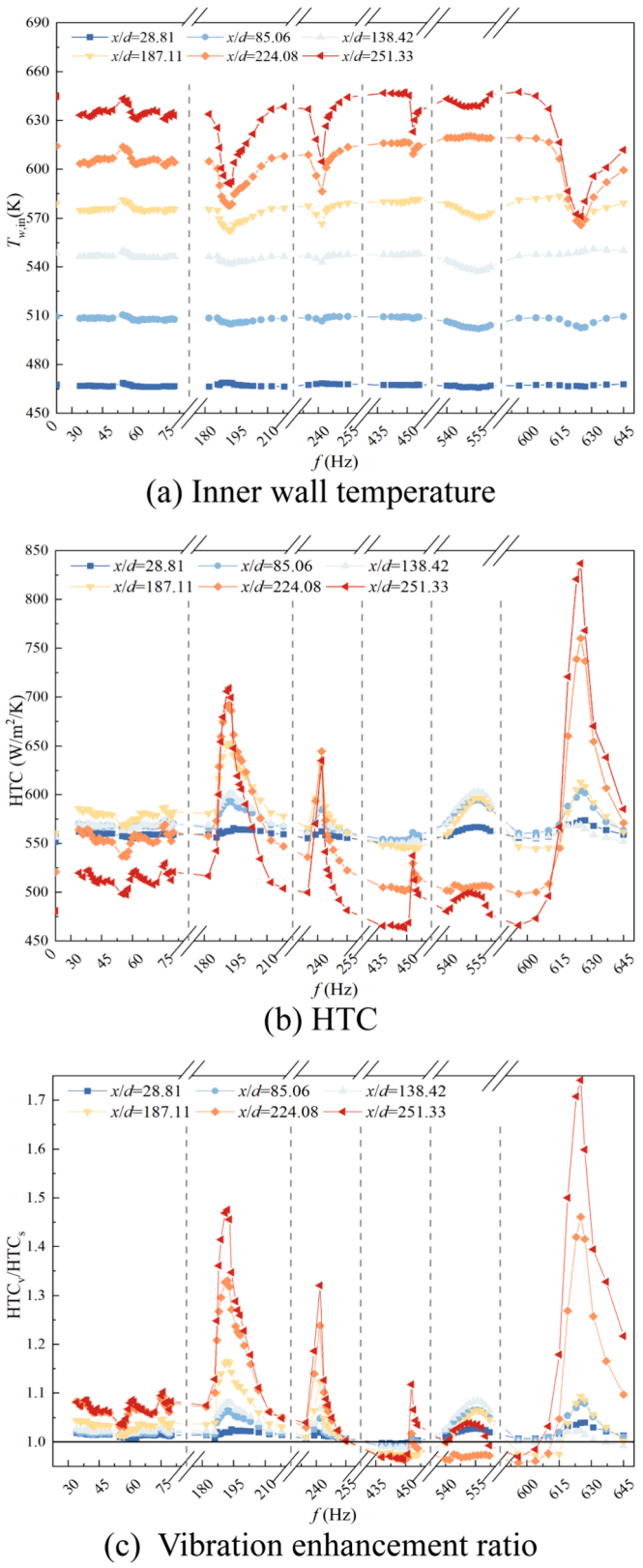

Fig. 13. Response of different parameters under various vibration frequency ranges of 20–80 Hz and 180–650 Hz (The dashed lines represent the folded frequency range with no apparent effects).

$$Nu = 0.5326Re^{0.27}Pr^{0.36}\left(\frac{\rho_w}{\rho_b}\right)^{-0.464}\left(\frac{\mu_w}{\mu_b}\right)^{0.116}\left(\frac{c_{p,m}}{c_{p,b}}\right)^{0.408} \quad (20)$$

where $c_{p,m} = \frac{H_w - H_b}{T_w - T_b}$, H_w and H_b represent the enthalpy of fuel at the inner wall temperature and bulk temperature, respectively. The relative deviation between experimental data and empirical correlation values of *Nu* is given in Fig. 14. With an average deviation of 11.8 %, the results demonstrate that the calculated values correlate well with the experimental ones. The 20 % error band and the 25 % error band are occupied by 83.7 % and 90 % of the experimental data, respectively.

Vibration affects heat transfer both directly and indirectly, and the indirect effect occurs through changes in buoyancy influenced by vibration. Therefore, when the influence of vibration is considered in the *Nu* correlation fitting, the thermal properties and vibration acceleration also need to be included. The influence of vibration frequency on heat transfer enhancement should be considered in relation to fluid–solid coupling characteristics. However, due to unclear patterns in how vibration frequency influences heat transfer, this study does not utilize experimental data from various vibration frequencies for fitting purposes. Instead, it relies solely on data obtained at a vibration frequency of 191 Hz. The empirical correlation for the vibration enhancement ratio in the laminar state is proposed in Eq. (21), based on data from the present study. The validation range of this empirical relation is Re = 300–2100 and g_v = 0–6 g. It can be explicitly seen from the correlation that the higher Re leads to the stronger vibration's impact on the heat transfer for the tubular laminar flow, in accordance with the previous analysis.

$$\frac{Nu_v}{Nu} = 1 + 0.000769Re^{0.81}\left(\frac{g_v}{g}\right)^{1.757}\left(\frac{\rho_w}{\rho_b}\right)^{-7.4}\left(\frac{\mu_w}{\mu_b}\right)^{4.9}\left(\frac{c_{p,m}}{c_{p,b}}\right)^{-4} \quad (21)$$

where subscript "v" represents the vibration condition.

Fig. 15 displays the relative deviations between the vibration enhancement ratios calculated using Eq. (21) and those obtained from experimental data. With an average deviation of 5.1 %, the predicted values correspond well with the experimental ones. The 20 % error band and the 10 % error band are occupied by 94.3 % and 84.8 % of the experimental data, respectively. The proposed correlation provides a valuable reference for predicting the heat transfer performance of supercritical pressure RP-3 in tubular laminar flow under vibration conditions. Moreover, it can also be seen from Fig. 15 that vibration has a significant heat transfer enhancement effect on supercritical RP-3 in a

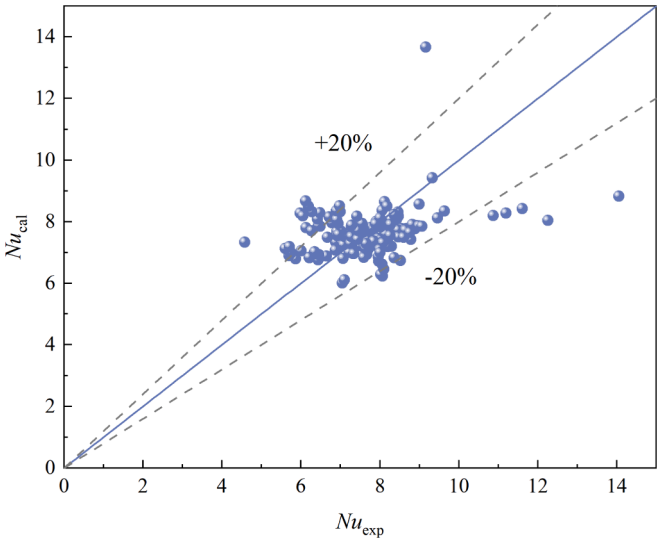

Fig. 14. Comparison between experimental *Nu* and empirical correlation values without vibration.

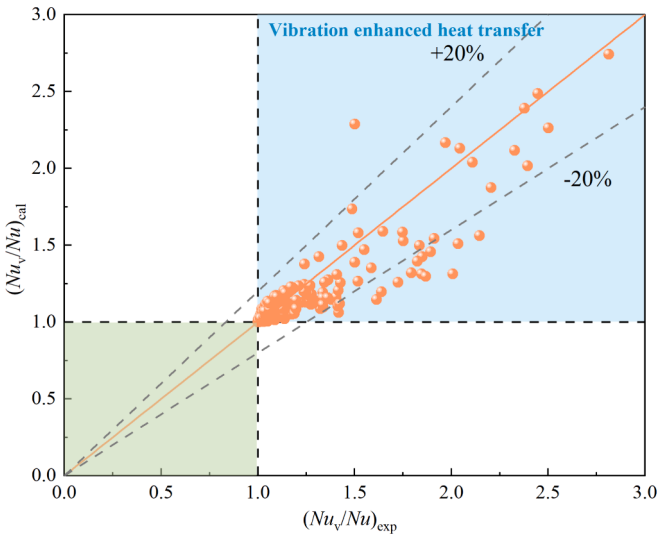

Fig. 15. Comparison between experimental Vibration enhancement ratio and empirical correlation values under vibration conditions.

horizontal tube of laminar flow.

5. Conclusions

In the current work, the heat transfer characteristics of supercritical pressure aviation kerosene RP-3 in a horizontal vibration tube under laminar conditions are discussed experimentally. The remarkable findings of this investigation can be obtained as follows.

i. Vibration could enhance the convective heat transfer under various system pressures (3–5 MPa), heat fluxes (36–108 kW/m^2), mass fluxes (117–273 kg/(m^2·s)), and fuel inlet temperatures (298–373 K) in the laminar regime. Vibration enhances the heat transfer along the tube by promoting momentum mixing between different layers in the laminar state and the higher *Re* can lead to a stronger enhancement effect. The maximum observed HTER across all experimental data is 2.8, occurring at $x/d = 224.1$ with the inlet temperature of 373 K.

ii. HTER hardly changes with system pressures ranging from 3 MPa to 5 MPa, exhibiting a maximum relative deviation of 3.9 % at different pressures. Heat transfer enhancement has a strong dependency on heat flux, as heat flux increases from 36 kW/m^2 to 108 kW/m^2, the average HTC increased by up to 36.4 %. For the effect of mass flux, HTER decreases with the increasing mass flux, owing to the combined effects of *Re* and buoyancy. As the inlet temperature increases, the peak vibration enhancement ratio also rises.

iii. Both the HTC and HTER monotonically rise with increasing vibration acceleration. The impact of the vibration frequency on the heat transfer is complex and related to fluid–solid coupling characteristics. Peak values in HTC and HTER are observed at frequencies of 625 Hz, 191 Hz, and 242 Hz, while the heat transfer deterioration occurs at 55 Hz, 445 Hz, and 604 Hz.

iv. Vibration effects on the thermal acceleration are minimal in laminar flow since the Kv is less than 3×10^{-6} for all experimental conditions. Furthermore, at high heat flux ($q = 108$ kW/m^2) and near the outlet region ($x/d > 196$), vibration can weaken the effect of buoyancy, resulting in at least an 18.3 % decrease in Gr_q/Gr_{th}.

v. Two *Nu* correlations with high accuracy for supercritical pressure RP-3 in tubular laminar flow under non-vibration and vibration conditions are proposed, and the 20 % error bands are occupied by 83.7 % and 94.3 % of the experimental data, respectively.

CRediT authorship contribution statement

Yanchen Fu: Methodology, Writing – review & editing, Funding acquisition. **Weitong Liu:** Writing – original draft, Formal analysis. **Juan Wang:** Writing – original draft, Data curation. **Lina Zhang:** Resources. **Jie Wen:** Supervision. **Hongwei Wu:** Writing – review & editing. **Guoqiang Xu:** Conceptualization, Project administration.

Declaration of competing interest

The authors declare that they have no known competing financial interests or personal relationships that could have appeared to influence the work reported in this paper.

Data availability

Data will be made available on request.

Acknowledgment

The authors appreciate the support from the National Science and Technology Major Project of China (Nos. J2019-III-0021-0065 and J2019-III-0015-0059), the Fundamental Research Funds for the Central Universities (No. 501XTCX2023146001), and the Science Center for Gas Turbine Project (No. P2022-C-II-005-001).

References

[1] A.S.J. van Heerden, D.M. Judt, S. Jafari, C.P. Lawson, T. Nikolaidis, D. Bosak, Aircraft thermal management: practices, technology, system architectures, future challenges, and opportunities, Prog. Aerosp. Sci. 128 (2022).
[2] L. Lv, J. Wen, Y. Fu, Y. Quan, J. Zhu, G. Xu, Numerical investigation on convective heat transfer of supercritical aviation kerosene in a horizontal tube under hyper gravity conditions, Aerosp. Sci. Technol. 105 (2020).
[3] W. Liu, G. Xu, Y. Fu, J. Wen, N. Zhang, Numerical investigation on forced, natural, and mixed convective heat transfer of n-decane in laminar flow at supercritical pressures, Int. J. Heat Mass Transf. 209 (2023).
[4] Y. Liu, G. Xu, Y. Fu, J. Wen, H. Huang, Thermal dynamic and failure research on an air-fuel heat exchanger for aero-engine cooling, Case Studies in Thermal Engineering 42 (2023).
[5] Y. Fu, W. Liu, H. Qi, Q. Chen, J. Wen, G. Xu, Heat transfer area optimization of intermediate heat-exchange cycle system for aero engines, Int. J. Heat Mass Transf. 220 (2024).
[6] Y. Fu, Y. Liu, J. Wang, Y. Wang, G. Xu, J. Wen, Local resistance characteristics of elbows for supercritical pressure RP-3 flowing in serpentine micro-tubes, Propul. Power Res. (2024).
[7] K.S.G. Krishnan, O. Bertram, O. Seibel, Review of hybrid laminar flow control systems, Prog. Aerosp. Sci. 93 (2017) 24–52.
[8] Z. Gao, Advanced Laminar Flow Aerodynamic Configuration Optimization Design for Green Aviation, in: 32nd AIAA Applied Aerodynamics Conference, 2014.
[9] F.A.A.A. Supplies, Academics, A. Supplies, I. Academics, U.S.D.o.T.F.A.A.F.S. Service, Aviation Maintenance Technician Handbook-powerplant, Aviation Supplies & Academics, 2012.
[10] R. Wagner, D. Maddalon, R. Clark, M. Hamamoto, R. Horstman, H. Cruver, High reynolds number hybrid laminar flow control (hlfc) flight experiment: Iv. suction system design and manufacture, in, Tech. Rep. NASA/CR-1999-209326, NASA Langley Research Center, Hampton, VA, 1999.
[11] Y. Fu, B. Bian, Y. Liu, L. Zhang, M. Li, J. Wen, G. Xu, Airside heat transfer analysis using Wilson plot method of three analogous serpentine tube heat exchangers for aero-engine cooling, Appl. Therm. Eng. 248 (2024).
[12] N. Colgan, G. Nellis, M. Anderson, Experimental measurement of the pressure drop and heat transfer characteristics of a crossflow heat exchanger in low-density flows, Int. J. Heat Mass Transf. 219 (2024).
[13] L. Zhuang, G. Xu, Q. Liu, M. Li, B. Dong, J. Wen, Superiority analysis of the cooled cooling air technology for low bypass ratio aero-engine under typical flight mission, Energ. Conver. Manage. 259 (2022).
[14] G.B. Bruening, W.S. Chang, Cooled cooling air systems for turbine thermal management, in: Turbo Expo: Power for Land, Sea, and Air, Vol. 78606, American Society of Mechanical Engineers, 1999, pp. V003T001A002.
[15] H. Kimura, M. Aritomi, Method for evaluation of effective forced-convective heat transfer rate associated with chemical heat absorption of heated fluid mixture: Part I, Int. J. Heat Mass Transf. 54 (2011) 2144–2153.
[16] H. Kimura, M. Aritomi, Method for evaluation of effective forced-convective heat transfer rate associated with chemical heat absorption of heated fluid mixture: Part II, Int. J. Heat Mass Transf. 54 (2011) 2703–2712.

[17] W. Liu, Q. Chen, The effect of transpiration cooling with liquid oxygen on the flow field, in: 34th AIAA/ASME/SAE/ASEE Joint Propulsion Conference and Exhibit, 1998, pp. 3515.
[18] W. Liu, Q. Chen, B. Wu, Transpiration cooling of rocket thrust chamber with liquid oxygen, in: 36th AIAA Aerospace Sciences Meeting and Exhibit, 2013, pp. 890.
[19] J.A. Scanlan, Effects of normal surface vibration on laminar forced convective heat transfer, Ind. Eng. Chem. 50 (1958) 1565–1568.
[20] R. Lemlich, Effect of vibration on natural convective heat transfer, Ind. Eng. Chem. 47 (1955) 1175–1180.
[21] R. Lemlich, M.A. Rao, The effect of transverse vibration on free convection from a horizontal cylinder, Int. J. Heat Mass Transf. 8 (1965) 27–33.
[22] S. Thapa, S. Samir, K. Kumar, S. Singh, A review study on the active methods of heat transfer enhancement in heat exchangers using electroactive and magnetic materials, Mater. Today:. Proc. 45 (2021) 4942–4947.
[23] Y. Lin, B. Farouk, Heat transfer in a rectangular chamber with differentially heated horizontal walls: effects of a vibrating sidewall, Int. J. Heat Mass Transf. 51 (2008) 3179–3189.
[24] M.-Y. Wen, Flow structures and heat transfer of swirling jet impinging on a flat surface with micro-vibrations, Int. J. Heat Mass Transf. 48 (2005) 545–560.
[25] S. Amiri, R. Taher, L. Mongeau, Quantitative visualization of temperature field and measurement of local heat transfer coefficient over heat exchanger elements in sinusoidal oscillating flow, Exp. Therm Fluid Sci. 85 (2017) 22–36.
[26] L. Cheng, T. Luan, W. Du, M. Xu, Heat transfer enhancement by flow-induced vibration in heat exchangers, Int. J. Heat Mass Transf. 52 (2009) 1053–1057.
[27] W. Liu, Z. Yang, B. Zhang, P. Lv, Experimental study on the effects of mechanical vibration on the heat transfer characteristics of tubular laminar flow, Int. J. Heat Mass Transf. 115 (2017) 169–179.
[28] A.M. Mohammed, S. Kapan, M. Sen, N. Celik, Effect of vibration on heat transfer and pressure drop in a heat exchanger with turbulator, Case Studies in Thermal Engineering 28 (2021).
[29] M. Ghalambaz, E. Jamesahar, M.A. Ismael, A.J. Chamkha, Fluid-structure interaction study of natural convection heat transfer over a flexible oscillating fin in a square cavity, Int. J. Therm. Sci. 111 (2017) 256–273.
[30] D.H. Kim, Y.H. Lee, S.H. Chang, Effects of mechanical vibration on critical heat flux in vertical annulus tube, Nucl. Eng. Des. 237 (2007) 982–987.
[31] F. Deaver, W. Penney, T. Jefferson, Heat transfer from an oscillating horizontal wire to water, (1962).
[32] W. Penney, T. Jefferson, Heat transfer from an oscillating horizontal wire to water and ethylene glycol, (1966).
[33] R. Hsieh, G. Marsters, Heat transfer from a vibrating vertical array of horizontal cylinders, Can. J. Chem. Eng. 51 (1973) 302–306.
[34] C. Guo, X. Hu, W. Cao, D. Yu, D. Tang, Effect of mechanical vibration on flow and heat transfer characteristics in rectangular microgrooves, Appl. Therm. Eng. 52 (2013) 385–393.
[35] A. Hosseinian, A.H. Meghdadi Isfahani, E. Shirani, Experimental investigation of surface vibration effects on increasing the stability and heat transfer coeffcient of MWCNTs-water nanofluid in a flexible double pipe heat exchanger, Exp. Therm Fluid Sci. 90 (2018) 275–285.
[36] L. Zhang, J. Lv, M. Bai, D. Guo, Effect of vibration on forced convection heat transfer for SiO2–water nanofluids, Heat Transfer Eng. 36 (2014) 452–461.
[37] Y. Zuo, H. Huang, Y. Fu, J. Wen, G. Xu, Vibration effects on heat transfer characteristics of supercritical pressure hydrocarbon fuel in transition and turbulent states, Appl. Therm. Eng. 219 (2023).
[38] A. Mitsuishi, M. Sakoh, T. Shimura, K. Iwamoto, A. Murata, H. Mamori, Direct numerical simulation of convective heat transfer in a pipe with transverse vibration, Int. J. Heat Mass Transf. 148 (2020).
[39] P. Moin, K. Mahesh, Direct numerical simulation: a tool in turbulence research, Annu. Rev. Fluid Mech. 30 (1998) 539–578.
[40] L. Rui, H. Tao, Numerical investigation of heat transfer and flow inner tube with periodically cosine oscillation, Int. J. Heat Mass Transf. 127 (2018) 1082–1091.
[41] H. Tao, L. Rui, W. Li, J. Cheng, Numerical study on effect of oscillation center position on heat transfer and flow internal tube, Int. J. Heat Mass Transf. 137 (2019) 799–808.
[42] M. Eesa, M. Barigou, Enhancing radial temperature uniformity and boundary layer development in viscous Newtonian and non-Newtonian flow by transverse oscillations: a CFD study, Chem. Eng. Sci. 65 (2010) 2199–2212.
[43] S. Tian, M. Barigou, An improved vibration technique for enhancing temperature uniformity and heat transfer in viscous fluid flow, Chem. Eng. Sci. 123 (2015) 609–619.
[44] W.-Y. Zhang, W.-W. Yang, Y.-H. Jiao, D.-W. Zhang, Numerical study of periodical wall vibration effects on the heat transfer and fluid flow of internal turbulent flow, Int. J. Therm. Sci. 173 (2022).
[45] Z. Yang, L. Ding, L. Zhang, L. Yang, H. He, Two degrees of freedom flow-induced vibration and heat transfer of an isothermal cylinder, Int. J. Heat Mass Transf. 154 (2020).
[46] H. Deng, C. Zhang, G. Xu, Z. Tao, B. Zhang, G. Liu, Density measurements of endothermic hydrocarbon fuel at sub-and supercritical conditions, J. Chem. Eng. Data 56 (2011) 2980–2986.
[47] H. Deng, K. Zhu, G. Xu, Z. Tao, C. Zhang, G. Liu, Isobaric specific heat capacity measurement for kerosene RP-3 in the near-critical and supercritical regions, J. Chem. Eng. Data 57 (2012) 263–268.
[48] G. Xu, Z. Jia, J. Wen, H. Deng, Y. Fu, Thermal-conductivity measurements of aviation kerosene RP-3 from (285 to 513) K at sub-and supercritical pressures, Int. J. Thermophys. 36 (2015) 620–632.
[49] H. Deng, C. Zhang, G. Xu, B. Zhang, Z. Tao, K. Zhu, Viscosity measurements of endothermic hydrocarbon fuel from (298 to 788) K under supercritical pressure conditions, J. Chem. Eng. Data 57 (2012) 358–365.
[50] A. Bejan, Convection heat transfer, John Wiley & Sons (2013).
[51] C. Zhang, H. Deng, G. Xu, W. Huang, K. Zhu, Enthalpy measurement and heat transfer investigation of RP-3 kerosene at supercritical pressure, Journal of Aerospace Power 25 (2010) 331–335.
[52] J. Jackson, M. Cotton, B. Axcell, Studies of mixed convection in vertical tubes, Int. J. Heat Fluid Flow 10 (1989) 2–15.
[53] J.D. Jackson, Fluid flow and convective heat transfer to fluids at supercritical pressure, Nucl. Eng. Des. 264 (2013) 24–40.
[54] C. Yang, J. Xu, X. Wang, W. Zhang, Mixed convective flow and heat transfer of supercritical CO2 in circular tubes at various inclination angles, Int. J. Heat Mass Transf. 64 (2013) 212–223.
[55] W.B. Hall, J. Jackson, Laminarization of a turbulent pipe flow by buoyancy forces, in: Mechanical Engineering, Vol. 91, ASME-AMER SOC MECHANICAL ENG 345 E 47TH ST, NEW YORK, NY 10017, 1969, pp. 66-&.
[56] B. Petukhov, A.F. Polyakov, V. Kuleshov, Y.L. Sheckter, Turbulent flow and heat transfer in horizontal tubes with substantial influence of thermogravitational forces, in: International Heat Transfer Conference Digital Library, Begel House Inc., 1974.
[57] J. Taylor, Introduction to error analysis, the study of uncertainties in physical measurements, 1997.
[58] A.S.U.s. Manual, Abaqus 6.11, http://130.149, 89 (2012) v6.
[59] O.A. Bauchau, J.I. Craig, Euler-Bernoulli beam theory, in: Structural analysis, Springer, 2009, pp. 173-221.
[60] D. McEligot, C. Coon, H. Perkins, Relaminarization in tubes, Int. J. Heat Mass Transf. 13 (1970) 431–433.
[61] K.O. Smith, Combustion instabilities in industrial gas turbines: solar turbines' experience, Prog. Astronaut. Aeronaut. 210 (2005) 29–41.
[62] H. Mongia, T. Held, G. Hsiao, R. Pandalai, Incorporation of combustion instability issues into design process: GE aeroderivative and aero engines experience, Prog. Astronaut. Aeronaut. 210 (2005) 43.
[63] W. Krebs, S. Bethke, J. Lepers, P. Flohr, B. Prade, C. Johnson, S. Sattinger, Thermoacoustic design tools and passive control: siemens power generation approaches, Prog. Astronaut. Aeronaut. 210 (2005) 89.
[64] E.N. Sieder, G.E. Tate, Heat transfer and pressure drop of liquids in tubes, Ind. Eng. Chem. 28 (1936) 1429–1435.
[65] K. Thulukkanam, Heat exchanger design handbook, CRC Press, 2013.
[66] F. Dittus, L. Boelter, Heat transfer in automobile radiators of the tubular type, Int. Commun. Heat Mass Transfer 12 (1985) 3–22.